Implementation of a CFD Model for Wall Condensation in the Presence of Non-Condensable Gas Mixtures

G. Vijaya Kumar[a,c], Liam M. F. Cammiade[a,b], Stephan Kelm[a,*], K. Arul Prakash[c], Eva M. Groß[a,b], Hans-Josef Allelein[a], Reinhold Kneer[b], Wilko Rohlfs[b]

[a] *Institute for Reactor Safety and Reactor Technology, Forschungszentrum Jülich, Jülich, Germany*
[b] *Institute of Heat and Mass Transfer, RWTH Aachen University, Aachen, Germany*
[c] *Department of Applied Mechanics, IIT Madras, Chennai, India*

Abstract

In this paper, we discuss a CFD model to predict vapor condensation on walls in the presence of non-condensable gases with a specific focus on large scale applications such as accidental flows in a nuclear reactor containment. Based on previous work, the dominant transport resistance is considered in the gaseous diffusion boundary layer, and the liquid film thermal resistance is insignificant; thereby, allowing the treatment of the two-phase wall condensation phenomenon as a single-phase (gas) phenomenon. For the numerical implementation, the *containmentFOAM* CFD package, based on OpenFOAM is used. For the first time, model implementation is discussed for arbitrary multi-component mixtures, and performances of two commonly used approaches—*Volumetric source terms* and *Face-fluxes*—are compared; the *Face-flux* model revealed to be more accurate, computationally cheaper, and less grid-dependent. Concluding, the *Face-flux* approach was validated against the experimental database for forced convection flows, obtained at the SETCOM facility in Forschungzentrum Jülich, Germany. The results demonstrate the model's predictiveness and robustness for a wide

*Corresponding author
Email addresses: vjykmr44@gmail.com (G. Vijaya Kumar), cammiade@wsa.rwth-aachen.de (Liam M. F. Cammiade), s.kelm@fz-juelich.de (Stephan Kelm), arulk@iitm.ac.in (K. Arul Prakash), gross@wsa.rwth-aachen.de (Eva M. Groß), h.j.allelein@fz-juelich.de (Hans-Josef Allelein), kneer@wsa.rwth-aachen.de (Reinhold Kneer), rohlfs@wsa.rwth-aachen.de (Wilko Rohlfs)

range of cases in the forced convection regime.

Keywords: CFD, wall condensation, containmentFOAM, non-condensable gases, boundary conditions, Stefan problem

---

Nomenclature

Greek symbols

α	laminar thermal diffusivity of the gas mixture ($\mathrm{m^2\,s^{-1}}$)
α_{eff}	effective thermal diffusivity of the gas mixture ($\mathrm{m^2\,s^{-1}}$)
α_k	thermal diffusivity of k^{th} gas species ($\mathrm{m^2\,s^{-1}}$)
α_t	turbulent thermal diffusivity of the gas mixture ($\mathrm{m^2\,s^{-1}}$)
δ	Kronecker delta
λ	laminar thermal conductivity of the gas mixture ($\mathrm{W\,m^{-1}\,K^{-1}}$)
λ_{eff}	effective thermal conductivity of the gas mixture ($\mathrm{W\,m^{-1}\,K^{-1}}$)
λ_k	thermal conductivity of k^{th} gas species ($\mathrm{W\,m^{-1}\,K^{-1}}$)
μ	dynamic viscosity of the gas mixture ($\mathrm{Pa\,s}$)
μ_k	dynamic viscosity of k^{th} gas species ($\mathrm{Pa\,s}$)
ν	kinematic viscosity of the gas mixture ($\mathrm{m^2\,s^{-1}}$)
ν_t	eddy viscosity ($\mathrm{m^2\,s^{-1}}$)
ω	turbulence eddy frequency ($\mathrm{s^{-1}}$)
ρ	density of the gas mixture ($\mathrm{kg\,m^{-3}}$)
τ	viscous stress tensor ($\mathrm{N\,m^{-2}}$)
τ_w	wall shear stress ($\mathrm{N\,m^{-2}}$)

Alphabets

$\vec{q}''$	heat flux vector ($\mathrm{W\,m^{-2}}$)
$\vec{q}''_{\mathrm{rad}}$	radiation heat flux vector ($\mathrm{W\,m^{-2}}$)
$\vec{g}$	gravity vector ($\mathrm{m\,s^{-2}}$)
$\vec{n}_i$	unit outward facing normal to the interface i
$\vec{S}_{\mathrm{mom}}$	volumetric source term for the momentum conservation equation ($\mathrm{N\,m^{-3}}$)
$\vec{U}$	mean velocity of the gas mixture ($\mathrm{m\,s^{-1}}$)
A_i	face area of the interface i ($\mathrm{m^2}$)
c_p	specific heat capacity of the gas mixture ($\mathrm{J\,kg^{-1}\,K^{-1}}$)
$c_{p,k}$	specific heat capacity of k^{th} gas species ($\mathrm{J\,kg^{-1}\,K^{-1}}$)
D_{jk}	binary diffusivity of the species pair $j-k$ ($\mathrm{m^2\,s^{-1}}$)
$D_{k,\mathrm{eff}}$	effective diffusivity of k^{th} gas species ($\mathrm{m^2\,s^{-1}}$)
$D_{k,m}$	molecular diffusivity of k^{th} gas species ($\mathrm{m^2\,s^{-1}}$)
$D_{k,T}$	thermal diffusion coefficient of k^{th} gas species ($\mathrm{kg\,m^{-1}\,s^{-1}}$)
$D_{k,t}$	turbulent diffusivity of k^{th} gas species ($\mathrm{m^2\,s^{-1}}$)
h	static enthalpy of the gas mixture ($\mathrm{J\,kg^{-1}}$)
h_k	specific enthalpy of k^{th} gas species ($\mathrm{J\,kg^{-1}}$)
h_L	heat transfer coefficient of the liquid film ($\mathrm{W\,m^{-2}\,K^{-1}}$)
$h_{\mathrm{ref},k}$	specific enthalpy of k^{th} gas species at T_{ref} ($\mathrm{J\,kg^{-1}}$)
HTC	heat transfer coefficient ($\mathrm{W\,m^{-2}\,K^{-1}}$)
J_k	diffusive mass flux of k^{th} gas species ($\mathrm{kg\,m^{-2}\,s^{-1}}$)
K	specific kinetic energy of the mean flow ($\mathrm{J\,kg^{-1}}$)

p	pressure (Pa)
Pr_t	turbulent Prandtl number, $Pr_t = 0.9$
R_i	thermal resistance at the liquid-vapor interface ($\mathrm{K\,m^2\,W^{-1}}$)
R_L	thermal resistance of the liquid film ($\mathrm{K\,m^2\,W^{-1}}$)
R_u	universal gas constant, $R_u = 8314.5\,\mathrm{J\,kmol^{-1}\,K^{-1}}$
S	list of all the gas species in the mixture
S_m	volumetric source term for the total mass conservation equation ($\mathrm{kg\,m^{-3}\,s^{-1}}$)
S_{Y_k}	volumetric source term for mass conservation equation equation of k^th species ($\mathrm{kg\,m^{-3}\,s^{-1}}$)
Sc_t	turbulent Schmidt number, $Sc_t = 0.9$
T	temperature (K)
T_ref	reference temperature (K)
u^+	dimensionless streamwise velocity
u_τ	friction velocity ($\mathrm{m\,s^{-1}}$), $u_\tau = \sqrt{\tau_w/\rho}$
v^+_suc	dimensionless suction velocity, $v^+_\mathrm{suc} = \vec{U}_i \cdot \vec{n}_i/u_\tau$
V_c	volume of the cell (control volume) adjacent to the interface i ($\mathrm{m^3}$)
W	molar mass of the gas mixture ($\mathrm{kg\,kmol^{-1}}$)
W_k	molar mass of k^th gas species ($\mathrm{kg\,kmol^{-1}}$)
x, y	Cartesian coordinates (m)
X_k	molar fraction or volume fraction of k^th gas species
y^+	dimensionless wall normal distance, $y^+ = yu_\tau/\nu$
Y_k	mass fraction of k^th gas species

$\dot{m}_i''$ condensation mass flux ($\mathrm{kg\,m^{-2}\,s^{-1}}$)

$\dot{m}_{k,i}''$ mass flux of k^{th} gas species at the condensing interface ($\mathrm{kg\,m^{-2}\,s^{-1}}$)

Ma Mach number of the fluid flow

Subscripts

b bulk of the fluid flow

c centre of the control volume adjacent to the condensing interface i

i condensing interface/wall

j, k indices of individual gas species

nc non-condensable gases

t turbulence component

v vapor/condensable gas species

w wall

L liquid film

sat vapor saturation condition

1. Introduction

In nuclear reactors, during a *Loss of coolant accident* (LOCA), steam condensation on containment structures is an effective heat transfer mechanism. It limits the pressurization of the containment or the efficiency of safety measures, e.g., the containment cooling system. Furthermore, wall condensation determines the flammability of the hydrogen-steam-air mixture. Consequently, wall condensation is of high relevance for ensuring the containment's integrity, which is the last barrier against the release of radioactive materials. In safety assessment, three-dimensional phenomena and local effects motivate the application of

Computational Fluid Dynamics CFD to containment atmosphere mixing complementary to established system codes. Thus, an accurate representation of wall condensation is crucial for CFD application. However, such a large-scale application also demands a numerically efficient and robust model formulation and implementation. Besides, wall condensation is an everyday phenomenon, e.g., fogging of a windshield, icing of a fridge, or humid walls in houses. There are also numerous engineering applications—in the chemical industry, ventilation systems (HVAC), and heat exchangers. For this reason, the present paper aims to discuss the model assumptions, its formulation, and implementation from a generic point of view and highlights assumptions with a specific focus on model application to containment atmosphere mixing.

Wall condensation rates can be estimated on the basis of engineering correlations, e.g., Chilton and Colburn (1934), Uchida et al. (1965), or Dehbi (2015), for various flow regimes and are integrated into the CFD model. However, in the context of nuclear safety, local effects are often of interest. The definition of 'bulk' conditions or a characteristic length scale is impossible, and the wall condensation rate needs to be calculated based on local quantities. As discussed in the theoretical background section (chapter 2) in detail, wall condensation of vapor in the presence of non-condensable gases differs from the condensation of pure vapor. While for the latter, the thermal resistance of the liquid film and at the liquid-vapor interface determines the condensation rate; the dominant heat transport resistance is in the gas phase in the presence of non-condensable gases (Peterson et al. (1993)). Therefore, the liquid phase can be neglected. The two-phase condensation simplifies into a single-phase (gas) phenomenon, with condensation rates being governed by the mass transport through the diffusion boundary layer. Such "diffusion-layer" models, based on the Stefan Problem, have been previously implemented in different CFD codes. For example, Zschaeck et al. (2014), using commercial CFD package ANSYS CFX, treats condensation of steam in the presence of air (non-condensable) by specifying mass flux at the wall. Dehbi et al. (2013) also discusses the same phenomenon but with volumetric source (sink) terms in the control-volumes adjacent to the

wall, with commercial CFD code, ANSYS Fluent. In the present work, the performance of the above two approaches—called from hereon as *Face-flux* and *Volumetric source terms*—is compared for the first time, to come up with the most robust method. The aforesaid models are implemented in the *containmentFOAM* CFD package (Kelm et al. (2019a), Kumar et al. (2020)), based on the open-source CFD code OpenFOAM-6.

Previous works limited their discussions to a binary gas mixture (steam-air). However, in real-life applications, vapor condensation occurs in the presence of more than one non-condensable gas species. To close this gap, in the current work, the models are presented for an arbitrary multi-component mixture—two or more species. Thus, the approaches discussed in this paper can be readily used for wall condensation modeling in other applications, as long as they meet the underlying model assumptions.

The paper is organized as follows: Section 2 discusses the wall condensation phenomenon and the assumptions made for simplifying the CFD model. Section 3 elaborates on the governing equations, their numerical treatment, and the algorithm of solving the equations. Section 4 compares the two wall condensation models—*Face-flux* and *Volumetric source terms*—for grid-dependence and mass conservation errors. Concluding, in chapter 5, a first model validation against the "**S**eparate **E**ffect **T**ests for **C**ondensation **M**odeling" (SETCOM) forced convection database (Kelm et al. (2019b)) is summarized to demonstrate its numerical stability and accuracy, for a steam-air mixture relevant to containment atmosphere mixing.

2. Theoretical background

2.1. Phenomenology of wall condensation

Vapor condenses on a wall, if the wall temperature falls below the local saturation temperature of vapor. Wall condensation happens through two modes: dropwise condensation and filmwise condensation. On non-wettable or hydrophobic surfaces, condensation takes place by formation of droplets. In film-

wise condensation, a continuous liquid film is formed and condensation occurs at the liquid-vapor interface. Further discussion in this paper is limited to filmwise condensation on hydrophilic surfaces.

In the case of pure vapor (Fig. 1a), the condensation mass and heat transfer rates are limited by the heat transfer resistance of the condensate film (R_L), the relative motion between the liquid and vapor phases (interfacial shear stress), and the interfacial thermal resistance. In the presence of non-condensable gases ($Y_{nc} > 10\%$), e.g., for a steam-air mixture, the steam mass transport through the diffusion boundary layer in the gas-phase adds another transport resistance (Fig. 1b).

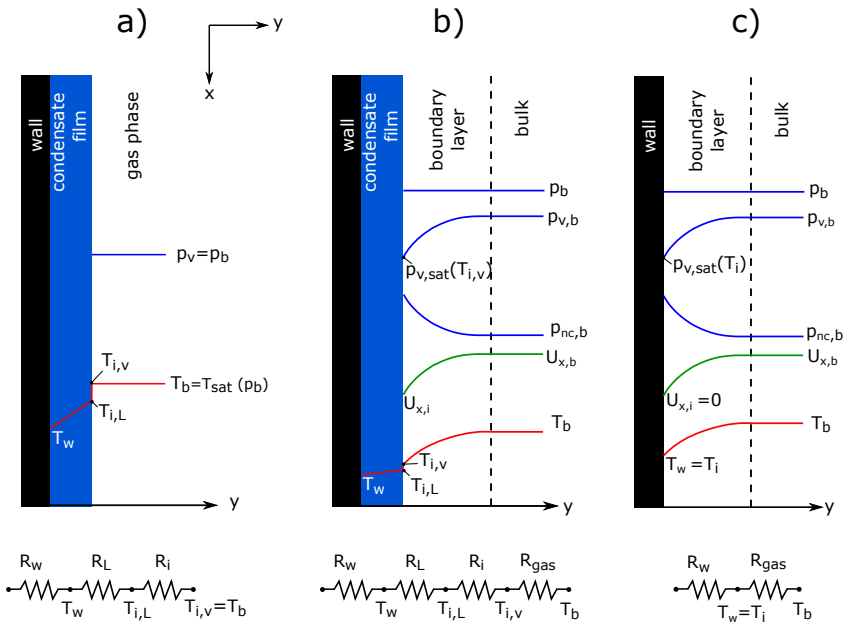

Figure 1: a) Film condensation of pure vapor, b) Film condensation of vapor in presence of non-condensable gas, and c) Simplified "diffusion-layer" model for vapor condensation in presence of non-condensable gas ($T_w = T_i$).

The factors affecting condensation are elaborated below.

Liquid film thermal resistance. The heat transport through the condensate depends on the liquid thermal conductivity and the film velocity (tangential to the wall). The downward motion of the film—governed by gravitational acceleration, inertial and viscous forces—enhances the heat transfer coefficient h_L and reducing resistance R_L.

Interfacial shear stress. The relative motion between the liquid and the gas phases causes shear forces at the interface, which results in momentum transfer between the phases. This affects the velocity of the condensate film, thereby influencing the liquid thermal resistance R_L and hence the condensation rates.

Interfacial thermal resistance. The net condensation rate is the difference between the evaporation and condensation processes occurring at the interface simultaneously (Huang et al. (2015)). From the kinetic theory of gases, the imbalance in these processes causes a temperature jump at the interface, i.e., $T_{v,i} \neq T_{L,i}$, and hence an additional thermal resistance R_i, as shown in Fig. 1b.

Presence of non-condensable gases. The vapor and the non-condensable gases are transported by convection and diffusion towards the interface, where the vapor condenses. The liquid-vapor interface is impermeable to non-condensable gases. Therefore, the convective mass flux of the non-condensables towards the interface will be compensated by a diffusive mass flux from the interface (and back into the domain). The diffusive mass flux is proportional to the concentration gradient of the non-condensable gases at the interface. A build-up of non-condensables at the interface, i.e., $Y_{nc} = 1 - Y_{v,\mathrm{sat}}$, arises. Consequently, the partial pressure of the vapor at the interface reduces and a corresponding reduction in saturation temperature ($T_{v,i}$) at which condensation occurs. The driving potential, $T_w - T_{v,i}$, reduces resulting in a net drop in the condensation heat flux (also mass flux).

2.2. State of the art

Nusselt (1916) studied the laminar filmwise condensation of saturated vapor on a vertical plate in a quiescent atmosphere, by a simple heat and mass bal-

ance analysis, ignoring the motion of the liquid condensate. Sparrow and Gregg (1959), extending on Nusselt's work, considered the inertia terms (advection) in the momentum and energy equation of the liquid, while neglecting the interfacial shear. The authors concluded that the condensation rates compared well with Nusselt's work and the addition of inertial terms had little impact. Koh et al. (1961), building on the work of Sparrow and Gregg (1959), modelled the interfacial shear and reported that it had infinitesimal significance on condensation for materials Prandtl numbers in the liquid phase around 1. Sparrow et al. (1967), based on the works of Koh (1962) and Cess (1960), concluded that interfacial shear, for a steam-air mixture, is of minor significance even for forced convection flows. Therefore, the motion of the liquid film and the shear stress at the liquid-vapor interface can be omitted in the model, i.e., no-slip velocity may be assumed at the liquid-vapor interface for the gas phase—$U_{x,i} = 0$. For natural convection flows, Minkowycz and Sparrow (1966) found that once non-condensables are present, even as low as 0.5%, the major transport resistance to condensation is in the diffusion boundary layer and that the interfacial resistance becomes a second-order effect. Sparrow et al. (1967) concluded the same observation for forced convection flows. Corradini (1984) studied the turbulent film condensation in presence of non-condensables, and found that the liquid film heat transfer coefficient is one order higher in magnitude than that of the gas phase. Ambrosini et al. (2014) also summarized previous research that the liquid film's effect on condensation rates is negligible, at least for thin films. de la Rosa et al. (2009) reviewed previous works on the influence of bulk condensation in the boundary layer on the total wall heat transfer and concluded that the effect is of minor relevance for nuclear reactor containment application. Consequently, the condensate film and the fog formation near the condensing wall can be omitted; the two-phase filmwise condensation phenomenon simplifies to a single phase (gas) mass transport problem. Dehbi et al. (2013), Bucci et al. (2013), Zschaeck et al. (2014), and others (e.g. Ambrosini et al. (2014)) have used this approach with reasonable success.

2.3. Modeling assumptions

Concluding, on basis of the above discussions and with respect to conditions expected for our target application to nuclear reactor containment atmosphere mixing, the following assumptions can be justified and allow to simplify the CFD model.

- Interfacial thermal resistance—temperature jump at the liquid-vapor interface—is infinitesimal, i.e., $T_{L,i} = T_{v,i} = T_i$.
- Thermal resistance of the liquid film is neglected and the saturation conditions are calculated at wall temperature, i.e., $T_w = T_i$.
- The liquid film is considered to be stagnant with no relative motion between the liquid and vapor phase, i.e., no-slip tangential velocity boundary condition is imposed for the gas phase at the wall ($U_{x,i} = 0$).
- The liquid-vapor interface is impermeable to non-condensable gases (Stefan's approach).
- There exists only one condensable species in the considered pressure and temperature range.
- Since the liquid film is neglected, the vapor which condenses on the wall is removed from the computational domain, meaning, no accumulation of liquid and its subsequent re-evaporation from the wall is modelled.
- Fog formation in the boundary layer is neglected.

As shown in Fig. 1c the model can be simplified to estimate the wall condensation rate by means of the mass transport in the diffusion boundary layer of the gas phase only.

3. CFD modelling

In the recent years, at Forschungzentrum Jülich, the *containmentFOAM* CFD solver and supporting model libraries, based on OpenFOAM, are being developed, to model containment flows (Kelm et al. (2019a) & Kumar et al. (2020)). During a severe accident, e.g., a LOCA (Loss of coolant accident) with core damage, the flow prevailing in a nuclear-reactor containment comprises of a multi-component gas mixture (in particular N_2, O_2, H_2, and H_2O) and it is primarily in the turbulent mixed convection regime. The flow is incompressible from the perspective of its speed, i.e., $Ma < 0.3$, but the density varies due to temperature gradients and mass concentration gradients of the multi-component mixture. Thus, the Boussinesq approximation for buoyancy forces becomes untenable, and the ideal gas equation of state models the varying density. Conjugate heat transfer modeling addresses condensation on cold structures of the containment (steel and concrete walls). Furthermore, the *containmentFOAM* solver can handle radiative heat transfer between the structures and the humid atmosphere. Due to the containment size (Volume $\sim$ 50,000 - 70,000 m^3 for a typical pressurized water reactor and Volume $\sim$ 15,000 m^3 for a boiling water reactor), scale resolving approaches such as LES or DNS becomes computationally expensive; therefore, an unsteady RANS (U-RANS) approach based on the $k-\omega-SST$ model by Menter and Esch (2001) is applied.

The CFD modeling section is organized into three parts: First, the equations governing the fluid flow are addressed. The second part discusses the different approaches for modeling wall condensation. Finally, the numerical methods and the order of solving the equations are elaborated.

3.1. Governing equations

3.1.1. Species mass conservation

For a system of N gas species with $S = \{1, 2, 3, ..., N\}$, the species mass conservation equation is defined in terms of the species mass fractions Y_k, $\forall k \in S$. Subscript v denotes the condensable species or vapor. The set of non-

condensable gas species, identified by subscript nc, includes all the species except the vapor.

$$\frac{\partial\left(\rho Y_k\right)}{\partial t} + \nabla \cdot \left(\rho \vec{U} Y_k\right) = -\nabla \cdot J_k + S_{Y_k}, \tag{1}$$

where $\vec{J_k}$ is the diffusive mass flux and S_{Y_k} is volumetric source term (= 0 unless explicitly defined) of the k^{th} specie. The diffusive mass flux $\vec{J_k}$ is described by Fick's law of diffusion

$$\vec{J_k} = -\rho D_{k,\text{eff}} \nabla Y_k - D_{k,T} \frac{\nabla T}{T}. \tag{2}$$

The first term on the RHS of Eq. (2) is the diffusive mass flux due to the concentration gradient. $D_{k,\text{eff}} = D_{k,m} + D_{k,t}$ is the effective diffusivity of the specie k in the multi-component gas medium with $D_{k,m}$ and $D_{k,t}$ being the molecular diffusivity and turbulent diffusivity respectively. In flow regimes, where turbulence dominates, it is common to assume the same molecular diffusivity for all the species. This approximation is suitable for gases of similar molecular weights. In containment applications, the molecular weights of the gases—H_2, H_2O, and N_2—are dissimilar, and they diffuse at different rates. Thus, in the present work, the *effective binary diffusivity approximation*, which handles the varying diffusion rates, is used to model the molecular diffusivity,

$$D_{k,m} = \frac{1 - X_k}{\sum_{\substack{j=1 \\ j \neq k}}^{N} X_j / D_{jk}}, \tag{3}$$

where X_j is the molar fraction of species 'j' and D_{jk} is the binary diffusivity of the species pair $j - k$. Turbulent diffusivity is defined as $D_t = \nu_t / Sc_t$, where ν_t is the eddy viscosity and $Sc_t = 0.9$ is the turbulent Schmidt number. The second term, on the RHS of Eq. (2), corresponds to mass diffusion due to temperature gradients i.e., thermophoresis or the Soret effect, where $D_{T,k}$ is the thermal diffusion coefficient of k^{th} species. For the wall condensation phenomenon, the mass diffusion is primarily governed by the gas concentration gradient, whereas the temperature gradient has a negligible impact (Minkowycz and Sparrow (1966)). Consequently, the effect of thermophoresis is omitted in the present work.

3.1.2. Total mass conservation

Summing the N species mass conservation equations (Eq. (1)) gives the total mass conservation or continuity equation

$$\frac{\partial \rho}{\partial t} + \nabla \cdot \left(\rho \vec{U}\right) = S_{\mathrm{m}}, \tag{4}$$

where S_{m} is the volumetric source term in the continuity equation ($S_{\mathrm{m}} = 0$, unless specified). The continuity equation is solved along with $N-1$ species mass conservation equations. The mass fraction of the N-th species (non-condensable species that is in abundance) is obtained by the mass fraction constraint, i.e., $\sum_{i=1}^{N} Y_k = 1$.

3.1.3. Momentum conservation equation

The momentum conservation equation that governs the flow velocity $\vec{U}$ is given by

$$\frac{\partial \left(\rho \vec{U}\right)}{\partial t} + \nabla \cdot \left(\rho \vec{U} \otimes \vec{U}\right) = -\nabla p + \nabla \cdot \tau + \rho \vec{g} + \vec{S}_{\mathrm{mom}}, \tag{5}$$

where τ is the viscous stress tensor, p is the pressure, $\vec{g}$ is the acceleration due to gravity, and $\vec{S}_{\mathrm{mom}}$ is the volumetric source term for the momentum equation ($\vec{S}_{\mathrm{mom}} = 0$, unless specified). The viscous stress tensor is defined as

$$\tau = \rho \left(\nu + \nu_t\right) \left[\nabla \vec{U} + (\nabla \vec{U})^T - \frac{2}{3}\delta \nabla \cdot \vec{U}\right], \tag{6}$$

where ν is the kinematic viscosity of the gas mixture, ν_t is the turbulent eddy viscosity and δ is the Kronecker delta. Turbulence model provides ν_t as described in section 3.1.6.

3.1.4. Energy conservation equation

Energy conservation is formulated in terms of the total energy equation for the static enthalpy h,

$$\begin{aligned} &\frac{\partial(\rho h)}{\partial t} + \nabla \cdot (\rho \vec{U} h) + \frac{\partial(\rho K)}{\partial t} + \nabla \cdot (\rho \vec{U} K) = \\ &\frac{\partial p}{\partial t} - \nabla \cdot \vec{q}'' + \nabla \cdot (\vec{U} \cdot \tau) + \vec{U} \cdot (\rho \vec{g}) + \vec{U} \cdot \vec{S}_{\mathrm{mom}} - \nabla \cdot \vec{q}''_{\mathrm{rad}} + S_{\mathrm{h}}. \end{aligned} \tag{7}$$

The LHS corresponds to the material derivative of total enthalpy, given by $h_{\text{tot}} = h + K$, with $K = |\vec{U}|^2/2$ being the mechanical energy (specific kinetic energy of the mean flow). The terms in the RHS are described as follows: The first term ($\partial p/\partial t$) accounts for the enthalpy changes due to temporal pressure variations. The second term corresponds to the enthalpy transport from net heat flux due to conduction and mass diffusion ($\vec{q}''$ described in Eq. (8)). The third term accounts for viscous dissipation; it is negligible for low speed flows, i.e., $Ma < 0.3$ and hence neglected. The fourth term and the fifth terms represent the work due to the momentum sources $\rho\vec{g}$ and $\vec{S}_{\text{mom}}$. The sixth term $-\nabla \cdot \vec{q}''_{\text{rad}}$ is the volumetric source term due to radiation heat transfer. The seventh term is for any arbitrary volumetric enthalpy source term ($S_{\text{h}} = 0$, unless specified). The heat flux vector,

$$\vec{q}'' = -\lambda_{\text{eff}} \nabla T + \sum_{k=1}^{N} \vec{J}_k h_k - \sum_{j=1}^{N} \sum_{k=1}^{N} \frac{p}{\rho^2} \frac{D_{T,j}}{Y_j} \frac{X_j X_k}{D_{jk}} \left(\frac{\vec{J}_k}{Y_k} - \frac{\vec{J}_j}{Y_j} \right), \tag{8}$$

consists of three contributions: 1) the conductive heat flux, 2) enthalpy transport due to diffusive mass flux, and 3) heat flux due to the Dufour effect. The Dufour effect is an inverse phenomenon of the Soret effect described in section 3.1.1, i.e., a heat flux arising due to mass concentration gradients. Minkowycz and Sparrow (1966) concluded that the Dufour effect has a negligible impact on wall condensation for a steam-air mixture—ergo, the heat flux contribution due to the Dufour effect is omitted in the present work. However, in the future, consideration has to be given to the Dufour and Soret effects in the presence of light gases, e.g., H_2, He. The diffusive heat flux follows Fourier's law of heat conduction. For improving the CFD solver's numerical stability, the diffusive heat flux term is formulated partly implicit by rewriting it in terms of static enthalpy h. From the preceding arguments and substituting for the diffusive mass flux (Eq. (2)), the heat flux vector becomes

$$\vec{q}'' = -\rho \alpha_{\text{eff}} \nabla h + \sum_{k=1}^{N} \rho \left(\alpha_{\text{eff}} - D_{k,\text{eff}} \right) h_k \nabla Y_k, \tag{9}$$

where $\alpha_{\text{eff}} = \alpha + \alpha_t$ is the effective thermal diffusivity of the gas mixture. Here, α is the molecular or laminar thermal diffusivity of the mixture and $\alpha_t = \nu_t / Pr_t$

is the turbulent thermal diffusivity. In the present work, the turbulent Prandtl number is chosen to be the same value as turbulent Schmidt number, i.e., $Pr_t = Sc_t = 0.9$. Consequently, the turbulence contribution in the second term of heat flux vector (Eq. (9)) vanishes and only the laminar part remains. Only if Lewis number $Le_k = \alpha / D_{k,m} \sim 1$ holds for all species, the second term in the heat flux vector (Eq. (9)) becomes negligible. Therefore, the heat flux vector is used as in Eq. (9) without further simplifications.

3.1.5. Equation of state

The transport equations of mass, momentum and energy are closed by the equations of state for density and enthalpy. For containment flows, the gas mixture is considered to be an ideal gas. Consequently, density is defined as

$$\rho = \frac{pW}{R_u T}, \tag{10}$$

where $W = \left(\sum_{k=1}^{N} Y_k / W_k \right)^{-1}$ is the molar mass of the gas mixture with W_k being the molar mass of the k^{th} species in $\mathrm{kg\,kmol^{-1}}$ and $R_u = 8314.5\,\mathrm{J\,kmol^{-1}\,K^{-1}}$ is the universal gas constant. With the ideal gas assumption, the static enthalpy for a gas species k is related to temperature by

$$h_k = h_{\text{ref},k} + \int_{T_{\text{ref}}}^{T} c_{p,k} dT, \tag{11}$$

where T_{ref} is the reference temperature, $h_{\text{ref},k}$ is the enthalpy of the k^{th} at the reference temperature, and $c_{p,k}$ is the specific heat capacity at constant pressure for species k (temperature-dependent property). The value of $T_{\text{ref}} = 0$ K and $h_{\text{ref},k} = 0\ \mathrm{J\,kg^{-1}}$ is used for all the gas species including the condensing vapor. Since bulk condensation is ignored and only wall condensation is under consideration in the present work, the phase-change enthalpy of condensation is handled through the boundary conditions (described in section 3.2.1). From this, the static enthalpy of the mixture is related to the temperature as $\frac{dh}{dT} = c_p$; with this relation, the temperature field results from static enthalpy using the Newton-Raphson method.

3.1.6. Turbulence quantities

Turbulence contribution arises in the species mass conservation, momentum conservation, and energy conservation equations through the turbulent mass diffusivity $D_{k,t}$, the eddy viscosity ν_t, and the turbulent thermal diffusivity α_t, respectively. The standard $k-\omega-SST$ model of Menter and Esch (2001), which solves transport equations for turbulent kinetic energy k[1]and eddy frequency ω, models turbulence. The model is selected because it can be integrated up to the wall with a low Reynolds number boundary condition (low-Re BC). The eddy viscosity ν_t is a function of k and ω. Further, D_t and α_t are evaluated from ν_t using relations discussed already.

3.1.7. Temperature dependent mixture properties

In a low-Re approach, the molecular transport properties dominate the wall fluxes; since strong temperature gradients exist in the vicinity of a condensing wall, temperature-dependent transport properties are important to obtain the correct mass, momentum, and energy fluxes. Individual species properties—molecular viscosity μ_k, thermal conductivity λ_k, and specific heat capacity at constant pressure $c_{p,k}$—are defined as polynomial functions of temperature. Temperature-dependent molecular diffusivity $D_{k,m}$ is specified by computing the binary diffusivity D_{jk} with the Fuller approach (Fuller et al. (1966)). Wilke (1950) model is used to define the gas mixture's viscosity and thermal conductivity. In contrast, the mixture's specific heat capacity is obtained with a mass-weighted summation of individual species' specific heat capacity values.

3.2. Wall condensation modelling

Wall condensation is enabled, if the value of saturation pressure of vapour at the interface temperature T_i is less than that of the wall adjacent cell, i.e., $p_{v,\text{sat}} < p_{v,c}$. Saturation pressure is computed at the interface temperature

[1] k used in section 3.1.6 identifies turbulent kinetic energy and not the species index k used in other sections

using Antoine's equation (Antoine (1888)). For steam, saturation pressure is given as

$$p_{v,\text{sat}} = 133.28Pa \cdot e^{\left(18.3036 - \frac{3816.44K}{T_i - 46.13K}\right)}. \tag{12}$$

The mass fraction of vapor at the interface corresponding to $p_{v,\text{sat}}$ is evaluated as follows:

1. Compute molar fraction of vapor using the *Dalton's law of partial pressures*, i.e., $X_{v,i} = p_{v,\text{sat}}/p_i$.
2. Calculate the effective molecular weight of the mixture of non-condensable species, i.e., $W_{nc,i} = \sum_{k\in nc} X_k^* W_k$. Since, the sum of the molar fractions of non-condensable gases is not equal to unity, a normalized molar fraction—$X_k^* = X_k / \sum_{j\in nc} X_j$—is used.
3. Find the effective molecular weight of the mixture of condensable and non-condensable gas species, i.e., $W_{\text{mix},i} = X_{v,i} W_v + (1 - X_{v,i})\, W_{nc,i}$.
4. Evaluate vapor mass fraction $Y_{v,i} = X_{v,i} W_v / W_{\text{mix},i}$.

If $p_{v,\text{sat}} \geq p_{v,c}$, to prevent re-evaporation of the vapor from the wall, a zero-flux or zero-gradient boundary condition is resembled by setting the vapor mass fraction at the interface equal to that of the wall adjacent cell .

If the condensation criterion is satisfied, vapor diffuses towards the cold wall (also the liquid-vapor interface). This motion also entrains the non-condensable gases; the liquid-vapor interface is impermeable to the non-condensable gases. In the vicinity of the interface, non-condensable gases will build-up. For both the condensing vapor and non-condensable gases, the mass flux normal to the interface—going out of the computational domain—has a convective and diffusive component. If $\vec{n}_i$ is the unit outward-facing normal to the interface, the mass flux for the condensable vapor is given by

$$\dot{m}''_{v,i} = \left(\rho_i \vec{U}_i Y_{v,i}\right) \cdot \vec{n}_i + \vec{J}_{v,i} \cdot \vec{n}_i. \tag{13}$$

Due to the impermeability condition, the mass flux of the non-condensable species is zero, i.e.,

$$\dot{m}''_{k,i} = \left(\rho_i \vec{U}_i Y_{k,i}\right) \cdot \vec{n}_i + \vec{J}_{k,i} \cdot \vec{n}_i = 0, \quad \forall k \in nc. \tag{14}$$

Equation (14) signifies that the convective flow of non-condensable gases towards the interface compensates the diffusive flux back into the bulk, due to the mass fraction of non-condensable species at the interface being more abundant than that of the near-wall cell. The mass fraction of each non-condensable gas species at the condensing interface is obtained by solving equation (14). The general formulation of mixture mass flux at the interface is

$$\dot{m}''_i = \rho_i \vec{U}_i \cdot \vec{n}_i = \dot{m}''_{v,i} + \sum_{k \in nc} \dot{m}''_{k,i}. \tag{15}$$

From equations ((13)) to ((15)), the condensation mass flux is

$$\dot{m}''_i = \dot{m}''_{v,i} = \frac{1}{1 - Y_{v,i}} \left(\vec{J}_{v,i} \cdot \vec{n}_i \right). \tag{16}$$

3.2.1. Interface temperature boundary condition

Based on the scenario, interface temperature may be modelled in one of the following ways.

1. Fixed temperature or Dirichlet BC. If the condensing wall can be considered an infinite reservoir of heat, the latent heat of condensation will have a negligible impact on the wall temperature; therefore, a fixed value boundary condition is sufficient.

2. Conjugate heat transfer BC. If the condensing wall is at the interface of a solid and a fluid region, an additional heat diffusion equation is solved to account for the heat transport in the solid region. Then, the interface temperature is evaluated by performing the heat balance as follows. The vapor condenses at the liquid-vapor interface by releasing the latent heat of condensation. The heat flux due to condensation is given by

$$\dot{q}''_{\text{condensation},i} = \dot{m}''_i h_{vL}, \tag{17}$$

where $h_{vL} = h_v - h_{l=L}$ is the latent enthalpy due to change of phase from vapor 'v' to liquid 'L' at the saturation pressure of vapor at the interface (Eq. (12)). The conjugate heat transfer boundary conditions is illustrated by means

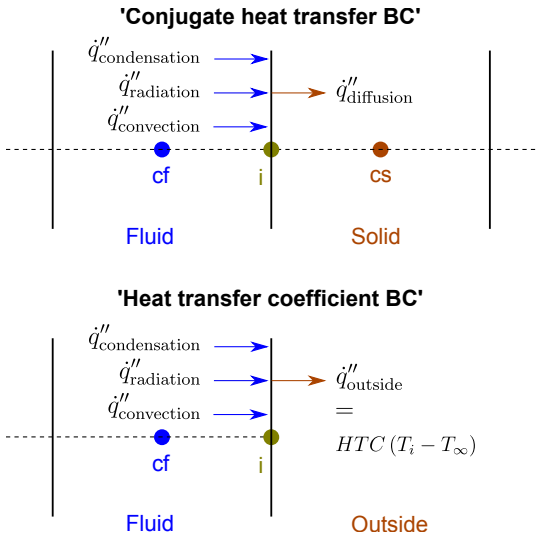

Figure 2: Temperature boundary conditions at the condensing interface 'i'—Conjugate heat transfer and Heat transfer coefficient—with heat flux due to convection, condensation and radiation.

of one-dimensional control-volumes in Fig. 2. The total heat flux from the fluid control-volume towards the interface is equal to the net heat flux from the interface into the solid control-volume. The heat flux from the fluid towards the interface has contributions due to condensation, radiation, and convection, whereas in the solid domain, the heat flux is only due to diffusion.

$$\dot{q}''_{\text{condensation},i} + \dot{q}''_{\text{radiation},i} + \lambda_{f,\text{eff}} \frac{T_{cf} - T_i}{\delta_{cf-i}} = \lambda_s \frac{T_i - T_{cs}}{\delta_{cs-i}}. \tag{18}$$

Here, $\lambda_{f,\text{eff}}$ is the effective thermal conductivity of the fluid at the interface accounting for laminar and turbulent heat flux, λ_s is the thermal conductivity of the solid, δ_{cf-i} is the distance of the cell-center 'cf' of the fluid control-volume from the interface i, and δ_{cs-i} is the distance of the cell-center 'cs' of the solid control-volume from the interface i. Temperature T_i is evaluated from Eq. (18) and applied as a boundary condition for the energy equations of the fluid and solid domain. The governing equations for the fluid and solid regions are solved in a segregated manner and iterated until the temperature and total heat flux

values at the interface converge for the fluid and solid regions.

3. Heat transfer coefficient BC. If a cooling system controls the wall temperature, e.g., oil/water-cooled heat exchanger, or if the interface is in contact with quiescent air, such that the heat transfer is by natural convection, then the heat transfer coefficient (HTC) and ambient temperature (T_∞) boundary condition can be employed. The interface temperature T_i is obtained by performing the following heat balance analysis.

$$\dot{q}''_{\text{condensation},i} + \dot{q}''_{\text{radiation},i} + \lambda_{f,\text{eff}} \frac{T_{cf} - T_i}{\delta_{cf-i}} = HTC\,(T_i - T_\infty) \tag{19}$$

3.2.2. Wall condensation models

In the literature, two approaches for modeling wall condensation are commonly used: 1) Volumetric source terms in the near-wall cell (Bucci et al. (2013) & Dehbi et al. (2013)), 2) Face-flux at the condensing wall (Zschaeck et al. (2014)). The mathematical description of the models is presented below, and their performances are compared in section 4.

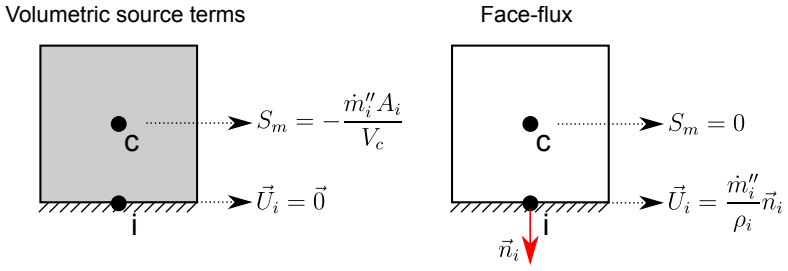

Figure 3: Illustration of *Volumetric source terms* (left) and *Face-flux* (right) models, with a two-dimensional control volume.

Approach 1: Volumetric source terms. In CFD codes, the use of a no-slip boundary condition defines a wall to be impermeable to mass flux. In this case, vapor condensation is implemented with volumetric source (sink) terms in the governing equations in the first cells adjacent to the walls (Fig. 3). The method

has been previously used in the works of Bucci et al. (2013) and Dehbi et al. (2013) with consistent results. The source term in the total mass conservation equation (Eq. (4)) for a cell-volume V_c and interface area A_i is given by

$$S_{\mathrm{m}} = -\frac{\dot{m}_i'' A_i}{V_c}. \tag{20}$$

Only the vapor condenses, and therefore it seems reasonable to introduce a source term only in the mass fraction equation of the vapor. But, for both the vapor and non-condensable species, concentration gradients at the wall result in non-zero diffusive mass flux. Consequently, the source terms of all species have to be corrected for this diffusive component and are of the form

$$S_j = -\frac{\dot{m}_i'' A_i}{V_c} Y_{j,i} = S_{\mathrm{m}} Y_{j,i}. \tag{21}$$

Along with the mass sink, the transported quantities have to be removed as well. The momentum source corresponding to the mass source term S_{m} is $\vec{S}_{\mathrm{mom}} = S_{\mathrm{m}} \vec{U}$. The respective source term in the energy equation is $\vec{S}_{\mathrm{mom}} \cdot \vec{U}$.

For the energy equation, Bucci et al. (2013) and Dehbi et al. (2013) considered the latent enthalpy of condensation in the source term. But, in the present work, the formulation of enthalpy of the vapor does not contain the latent heat of condensation (section 3.1.5). Instead, the latent heat is treated through the temperature boundary condition. Thus, the source term in the energy equation is obtained by summing the contributions from individual species as

$$S_{\mathrm{h}} = \sum_{j=1}^{N} S_j h_j = S_{\mathrm{m}} h. \tag{22}$$

Similarly, the source terms for the turbulent kinetic energy equation and eddy frequency equation are $S_{\mathrm{k}} = S_{\mathrm{m}} k$ and $S_\omega = S_{\mathrm{m}} \omega$, respectively. The source terms of the species mass fractions, momentum, enthalpy and turbulence equations are of form $S_\phi = S_{\mathrm{m}} \phi$, where ϕ is any arbitrary variable. Since, S_{m} is negative, the volumetric source terms are discretized as implicit terms, for better convergence.

Approach 2: Face-flux. Instead of a "no-slip" boundary condition for velocity, mass flux is defined at the interface by specifying a suction velocity normal to

the interface (Fig. 3).

$$\vec{U}_i = \frac{\dot{m}''_i}{\rho_i}\vec{n}_i \tag{23}$$

The above formulation also renders the velocity component tangential to the wall zero, i.e. $U_{x,i} = 0$. Through this boundary condition, the sink terms due to condensation, appear in the convective component $\nabla \cdot \left(\rho \vec{U} \phi\right)$ of all the governing equations, where $\phi \in \{1, Y_j, U, h, k, \text{and } \omega\}$.

3.2.3. Wall functions

In industrial applications, with large and complex geometries, it is impossible to fully resolve the turbulent boundary layer at all locations; instead, wall functions are employed to predict the wall fluxes. Though the wall condensation model developed in the current work, is for all the flow regimes—forced convection, natural convection, and mixed convection—, the discussion in this paper is limited to only forced convection flows for brevity's sake. Ideally, the wall functions should give mesh insensitive predictions, irrespective of whether the first grid point normal to the wall is in the viscous sublayer ($y^+ < 6$), or in the buffer layer ($5 < y^+ < 30$), or in the log-law region ($y^+ > 30$) of the forced convection turbulent boundary layer. Continuous wall functions achieve this purpose by blending the profiles of non-dimensional quantities—velocity, temperature, concentration, turbulent kinetic energy, and eddy frequency—in the viscous sublayer and the log-law region. In the absence of wall condensation, the turbulent viscosity at the wall ν_t is obtained from the Spalding (1961) continuous velocity profile (see Fig. 4). The Kader (1981) wall function gives the turbulent thermal diffusivity α_t and mass diffusivity D_t, based on the continuous profiles of temperature and species mass fractions. The eddy frequency ω value at the wall is specified through the blended profile described in Menter and Esch (2001). A zero-gradient boundary condition is imposed for the turbulent kinetic energy.

During condensation of vapor on a wall, the mass transport normal to the wall brings about the *suction effect*, which compresses the boundary layer, and hence the velocity profile deviates from the standard log-law profile (Favre et al.

(1966)). The strength of the condensation is quantified by the non-dimensional suction velocity $v^+_{\text{suc}} = \vec{U}_i \cdot \vec{n}_i / u_\tau$, where $u_\tau = \sqrt{(}\tau_w/\rho)$ is the friction velocity. Figure 4 shows the streamwise velocity (u^+) profiles for multiple suction velocities; it can be observed that the deviation from the log-law profile is more pronounced at larger suction velocities. Sucec (1999) and Lehmkuhl et al. (2016) describes corrected velocity profiles, as an alternative to the Spalding profiles, to handle this *suction effect*. However, for the experimental validation cases considered in the present work (section 5), the suction velocity $v^+_{\text{suc}} < 0.02$ Consequently, the u^+ deviation from the log-law profile is expected to be insignificant. Hence, the continuous wall functions, without corrections for the *suction effect*, are deemed applicable. Future work aims at implementing a new consistent wall treatment for near-wall suction and buoyancy effects (Kelm et al. (2019b)).

A summary of the boundary conditions at the condensation interface is given in Table 1.

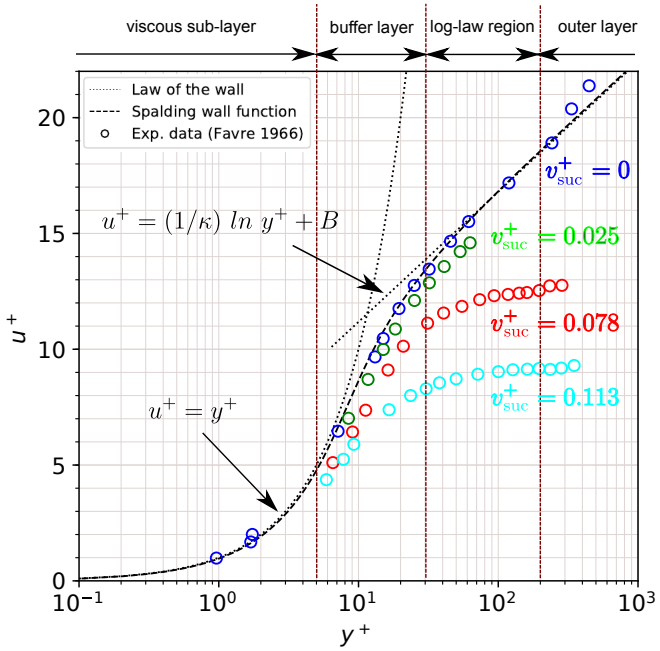

Figure 4: Streamwise velocity profiles for different suction velocities $v^+_{\rm suc}$, compared with the law of the wall ($\kappa = 0.41$, $B = 5.5$) and Spalding continuous velocity profile, for turbulent, forced convection flows.

Field	Boundary condition
Vapor mass fraction $Y_{v,i}$	Saturation condition at T_i
Non-condensable mass fractions $Y_{j,i}$	Impermeability condition (Eq: (14))
Velocity $\vec{U}_i$	No-slip condition for *Volumetric source terms* method /
	Suction velocity for *Face-flux* method (Eq: (23))
Temperature T_i	Fixed value /
	Conjugate heat transfer /
	Heat transfer coefficient
Turbulent viscosity $\nu_{t,i}$	Spalding profile (Spalding (1961))
Turbulent thermal diffusivity $\alpha_{t,i}$	Kader wall function (Kader (1981))
Turbulent mass diffusivity $D_{t,i}$	Kader wall function (Kader (1981))
Turbulent kinetic energy k_i	Zero gradient
Eddy frequency ω_i	Menter's profile (Menter and Esch (2001))

Table 1: Boundary conditions at the condensation interface.

3.3. Algorithm and solution method

The numerical discretization of the governing equations is second-order accurate in time and space. The transport equations are solved in a segregated manner until the convergence criterion (Initial residuals $< 10^{-5}$) is reached (Fig. 5). PIMPLE algorithm handles the pressure-velocity coupling in the momentum equation.

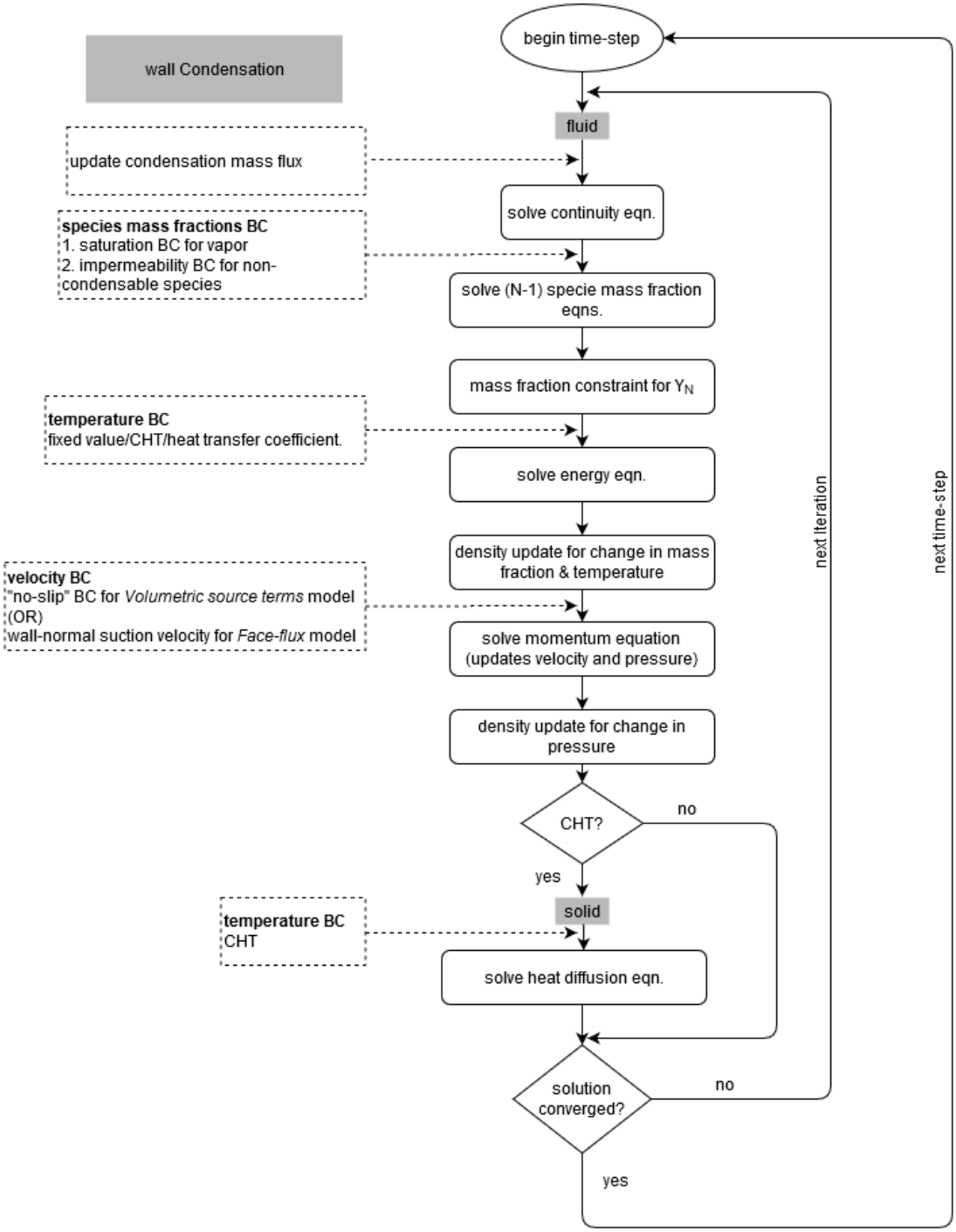

Figure 5: Wall condensation model interfacing with the PIMPLE algorithm for segregated solution of transport equations.

4. Comparison of *Volumetric source terms* and *Face-flux* approaches

The two approaches, *Volumetric source terms* and *Face-flux*, are compared based on convergence behavior, grid sensitivity, and mass conservation of the gas species. Due to its simplicity, a 2D turbulent channel flow with two species—steam (H_2O) as the vapor and air as the non-condensable gas—is chosen. The channel is 6 m in length (x-axis) and 0.45 m in height (y-axis) with an inlet at the left end and outlet at the right end. The top wall of the channel is adiabatic, while the bottom wall is the condensing interface with fixed temperature $T_i = 281.45$ K. The inlet boundary conditions are: $U = 4.89$ m/s, $T = 353.15$ K, $Y_{H_2O} = 0.3111$, and $Y_{Air} = 0.6889$. A turbulence intensity of 5% is used to define the turbulent kinetic energy k and eddy frequency ω at the inlet. The simulations are carried out for a physical time of 10 s, which amounts to more than eight flow passes[2], thereby achieving a steady-state.

Convergence behavior. The *Face-flux* method exhibited better convergence behavior and required 15% lesser computational time than the *Volumetric source terms* model.

Grid sensitivity. Two meshes with the first grid point normal to the wall placed in the viscous sub-layer ($y^+ \sim 1$ and total cells = 39,032) and log-law region ($y^+ > 30$ and total cells = 28,700), otherwise identical characteristics, are employed to study grid sensitivity. Due to the usage of continuous wall functions (section 3.2.3), grid-independent solutions are expected for both approaches. Figure 6 compares the wall quantities—total wall heat flux, convective wall heat flux, condensation mass flux, and wall shear stress—between the two approaches for $y^+ \sim 1$ and $y^+ > 30$ meshes. The effect of radiation heat transfer is omitted in the current work; therefore, the total wall heat flux only comprises two components, i.e., convective heat flux and latent heat flux of condensation.

[2] One flow pass = time taken for the fluid to move through the entire channel length with the inlet velocity (here 1.227 s).

The two methods exhibit nearly identical wall fluxes for the $y^+ \sim 1$ mesh. Even with $y^+ > 30$ mesh, the *Face-flux* method provides comparable results to the $y^+ \sim 1$ mesh, especially for the wall shear stress and condensation mass flux quantities. Though the convective wall heat flux values of the $y^+ > 30$ mesh deviate from the results of $y^+ \sim 1$ mesh, it is not unduly concerning. On a condensing wall, the latent heat flux of condensation—proportional to mass flux (Eq. (17))—overwhelms the convective component. Since the mass flux due to condensation is calculated in a grid-independently, the prediction of latent heat flux, and thus, the total heat flux is less sensitive to the near-wall grid resolution. On the other hand, the *Volumetric source terms* model showed strong grid dependence, with the results of $y^+ > 30$ mesh deviating significantly from the $y^+ \sim 1$ mesh.

Mass conservation. The total mass and individual species mass balance are critical properties for a CFD analysis. Here, the mass flow rate error for a species is the difference between the mass flow rate entering and leaving the computational domain. Steam enters via the inlet and leaves through the outlet and the condensation interface (Eq. (24)). Air being the non-condensable species, the error is defined as in Eq. (25).

$$\dot{m}_{H_2O,\text{error}} = |\dot{m}_{H_2O,\text{inlet}} - \dot{m}_{H_2O,\text{outlet}} - \dot{m}_{\text{condensation}}| \tag{24}$$

$$\dot{m}_{Air,\text{error}} = |\dot{m}_{Air,\text{inlet}} - \dot{m}_{Air,\text{outlet}}| \tag{25}$$

From Table 2, it becomes obvious that the species mass conservation is violated for the *Volumetric source terms* method on the $y^+ > 30$ mesh.

Grid-sensitivity and mass conservation errors with the *Volumetric source terms* approach can be understood by integrating the terms corresponding to condensation, over the control-volume. For an arbitrary transport variable ϕ, where $\phi \in U, Y_j, h, k$ and ω, the net quantity removed due to condensation with the *Volumetric source terms* approach is $\dot{m}_i'' A_i \phi_c$, whereas for the *Face-flux* method, the value is $\dot{m}_i'' A_i \phi_i$. The *Volumetric source terms* approach removes

transport quantities present at the first cell-center instead of the transport quantities at the condensing interface. Larger the distance of the first-grid point from the wall, greater is the miscalculation, and thus the grid-dependence and mass conservation errors.

Furthermore, the no-slip velocity condition at the interface with the *Volumetric source term* approach is unphysical, as it cannot capture the *suction effect* due to condensation. The *suction effect* causes the thinning of boundary layers—enhanced near-wall gradients—leading to increased mass, momentum, and heat transfer. Dehbi et al. (2013) proposed a modified correction factor to overcome this deficiency of the *Volumetric source terms* method. Such a correction is unnecessary for the *Face-flux* model, as the suction velocity, imposed on a condensing wall, captures the thinning of boundary layers.

In conclusion, the *Face-flux* approach was superior to *Volumetric source terms* on all counts: convergence behavior, grid-independence, and mass conservation. In addition to this, no correction is needed to account for the *suction effect*. Thus, the results discussed from hereon will be limited to the *Face-flux* model.

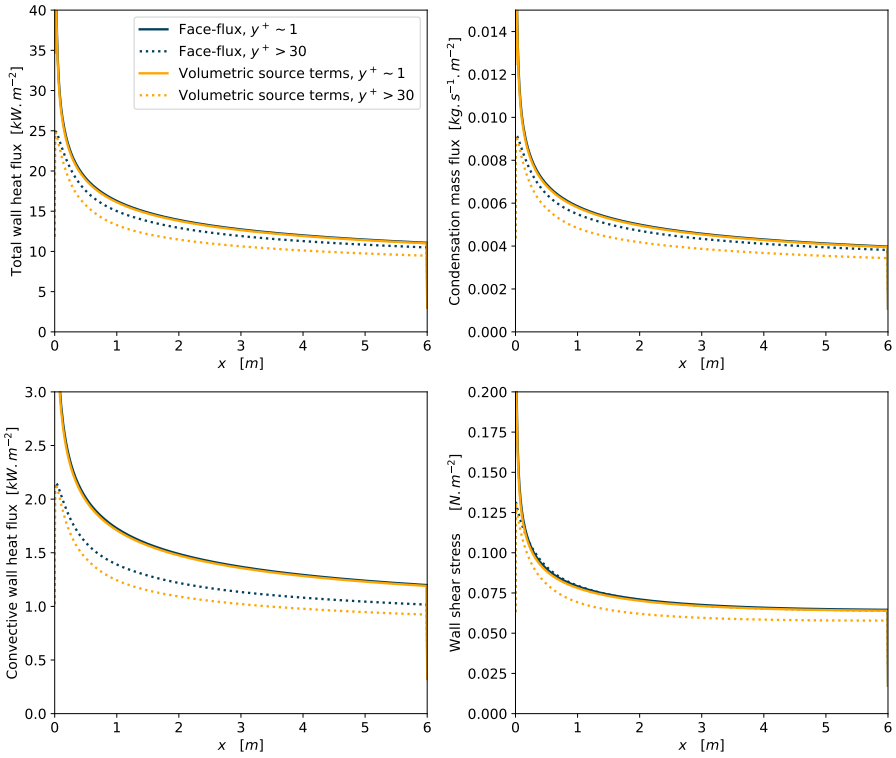

Figure 6: Grid sensitivity of the *Face-flux* and the *Volumetric source terms* models, based on local fluxes on the condensing wall: total wall heat flux (left top), condensation mass flux (right top), convective wall heat flux (left bottom), and wall shear stress (right bottom).

Model	Mesh	$\dot{m}_{H_2O,error}$ (% of $\dot{m}_i''$)	$\dot{m}_{Air,error}$ (% of $\dot{m}_i''$)
Face-flux	$y^+ \sim 1$	0	0
Face-flux	$y^+ > 30$	0	0
Volumetric source terms	$y^+ \sim 1$	0.8	0.8
Volumetric source terms	$y^+ > 30$	15	15

Table 2: Comparison of the species mass conservation errors for the *Volumetric source terms* and *Face-flux* wall condensation models on $y^+ \sim 1$ and $y^+ > 30$ meshes.

5. Model Validation

The *Face-flux* wall condensation model is validated against the experimental database obtained at the SETCOM facility.

5.1. SETCOM experimental facility

Figure 7 illustrates the setup of the SETCOM facility. The condensation channel is 6 m in length and comprises of three adiabatic sidewalls and a cooled aluminum plate (condensing wall). The adiabatic sidewalls have heated window cut-outs, at certain positions, for optical instrumentation. Type PT100 resistance thermometers measure wall temperatures inside the cooled aluminum plate, thus estimating wall heat fluxes. SETCOM facility's inclination angle can be seamlessly varied between 90°-0°, i.e., vertical position to horizontal position, thereby changing the angle of the gravitational acceleration to the flow stream and thus allowing for flow investigations in both the forced convection and mixed convection regimes. The test series on forced convection considered in the current work was conducted in a vertical position. Liquid coolant in the heat exchanger, which controls the condensing wall temperature, is at 281 K. Three steam generators, with a maximum total thermal power output of 150 kW, supply steam. Airflow from the blower passes through a pre-heater section and then takes a 180° turn, to pass through a flow straightener leading to the condensation channel. One of the SETCOM facility's primary objectives is to investigate wall condensation for a wide range of Reynolds and Grashof numbers; therefore, the bulk flow passing through the condensation channel can be kept to temperatures up to 100 °C, a relative humidity of up to 99 %, and an inlet velocity in the range of $0.5\,\mathrm{m\,s^{-1}}$ to $5\,\mathrm{m\,s^{-1}}$. Kelm et al. (2019b) describes the SETCOM facility in more detail.

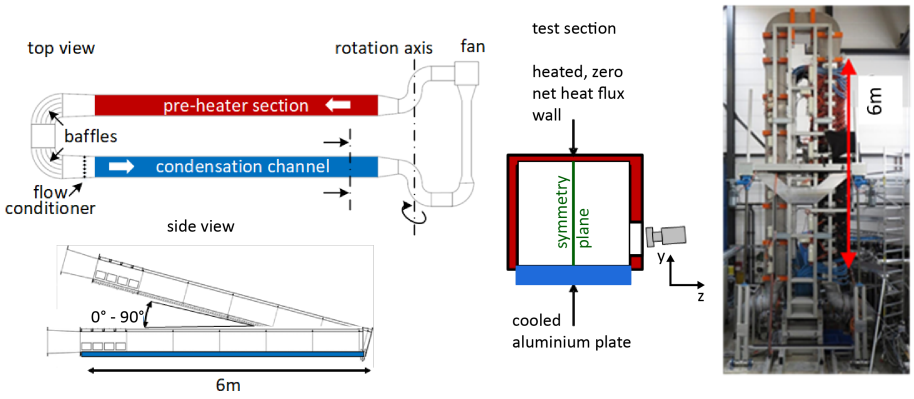

Figure 7: Schematic of the SETCOM facility (left), a photograph of the facility in vertical position.

5.2. Strategy

Accurate experimental measurements of the local condensation rate $\dot{m}_i''$ is required to validate the wall condensation model. With the available instrumentation in the SETCOM facility, the estimation of condensation mass flux directly from the steam concentration boundary layer is infeasible. Instead, the total heat flux, obtained by computing gradients of the measured wall temperatures in the cooled aluminum plate, provides a reasonable estimate of condensation mass flux[3].

To showcase the model validity for a broad range of condensation strengths, local wall fluxes are presented for three cases, representing a high (Case 1), medium (Case 2), and low (Case 3) condensation rate. Table 5.2 discusses the boundary conditions for the cases. Finally, the integral value of total heat flux obtained from the CFD model is compared against the experimental data for the entire forced convection SETCOM database, consisting of 81 cases, ranging between mild to severe condensation rates.

[3]For air-steam mixtures used in the current work, the latent heat flux is an order of magnitude larger the convective heat flux; hence, the total heat flux is a representative of

Name	U_{in} [m s^{-1}]	T_{in} [K]	$Y_{\text{H}_2\text{O,in}}$ [wt. fr]	$Y_{\text{H}_2\text{O,i}}$ [wt. fr]	Re	v^+_{suc}
Case 1	4.68	353.15	0.31	0.0092	$1.07 \cdot 10^5$	-0.0140
Case 2	2.98	343.15	0.19	0.0079	$6.96 \cdot 10^4$	-0.0081
Case 3	3.95	333.15	0.06	0.0062	$9.64 \cdot 10^4$	-0.0027

Table 3: Boundary conditions for the three representative cases with different condensation strengths (signified by v^+_{suc}). The steam mass fraction at the condensing wall ($Y_{\text{H}_2\text{O,i}}$) is evaluated from saturation conditions at the interface temperature (T_i).

5.3. Mesh

Figure 8 illustrates the overall meshing of the numerical domain and the near-wall grid refinement. The computational domain consists of the region downstream of the flow conditioner until the end of the cooling plate. Three-dimensional simulations of the entire experimental database are computationally cumbersome, and consequently, the flow is modeled with 2D block-structured meshes. The mesh is refined towards the domain inlet and beginning of the cooling plate, to capture the boundary layer development. To assess the validity of the wall functions (section 3.2.3), a fine mesh ($y^+ \sim 1$) and a coarse mesh ($y^+ \sim 75$) are considered. The cooled wall is modeled with the heat transfer coefficient boundary condition—effective $HTC \sim 1656\,\text{W/m}^2\text{/K}$ and $T_{\text{coolant}} = 280.65\,\text{K}$. Furthermore, the established *CFD best practise guidelines* (ERCOFTAC (2001)) are followed to minimize the numerical errors.

latent heat flux and consequently, the condensation mass flux.

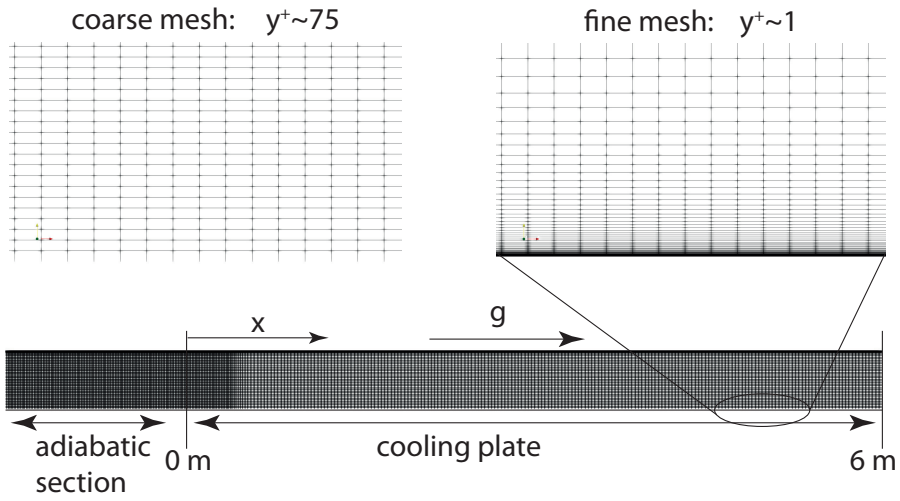

Figure 8: Two-dimensional computational domain of the SETCOM channel with different near-wall grid refinement for fine and coarse meshes.

5.4. Comparison with experimental data

5.4.1. Local wall fluxes

Figure 9 presents the CFD model's prediction of local wall fluxes, i.e., total wall heat flux, convective wall heat flux, and wall shear stress, on the condensing wall, for the three cases with different condensation rates, on both the fine and coarse meshes. The total heat flux values predicted with fine mesh compares very well with the experimental data for all three condensation scenarios. The coarse mesh solutions, with the first wall-normal grid point positioned in the log-law region, compared reasonably with the experimental data for $x > 3m$, where the boundary layer is developed. In the developing part of the flow, especially for $x < 1m$, the coarse mesh solution is visibly lower than the fine mesh solution; this is an expected behavior only, as the wall functions are primarily derived for fully-developed forced convection flows. No experimental data is available for the convective wall heat flux, and the wall shear stress values. Still, comparisons between the coarse and fine mesh solutions indicate similar deviations in the flow's developing part for the coarse mesh. The *suction effect* at the condensing

interface also impacts the coarse solution. Wall functions used in the current work are not corrected for this *suction effect* (section 3.2.3), thereby leading to an increased under-prediction in the wall fluxes for the coarse mesh as the condensation rate (suction velocity) increases. The effect of suction is more prominent in Case 1, with the highest condensation rate.

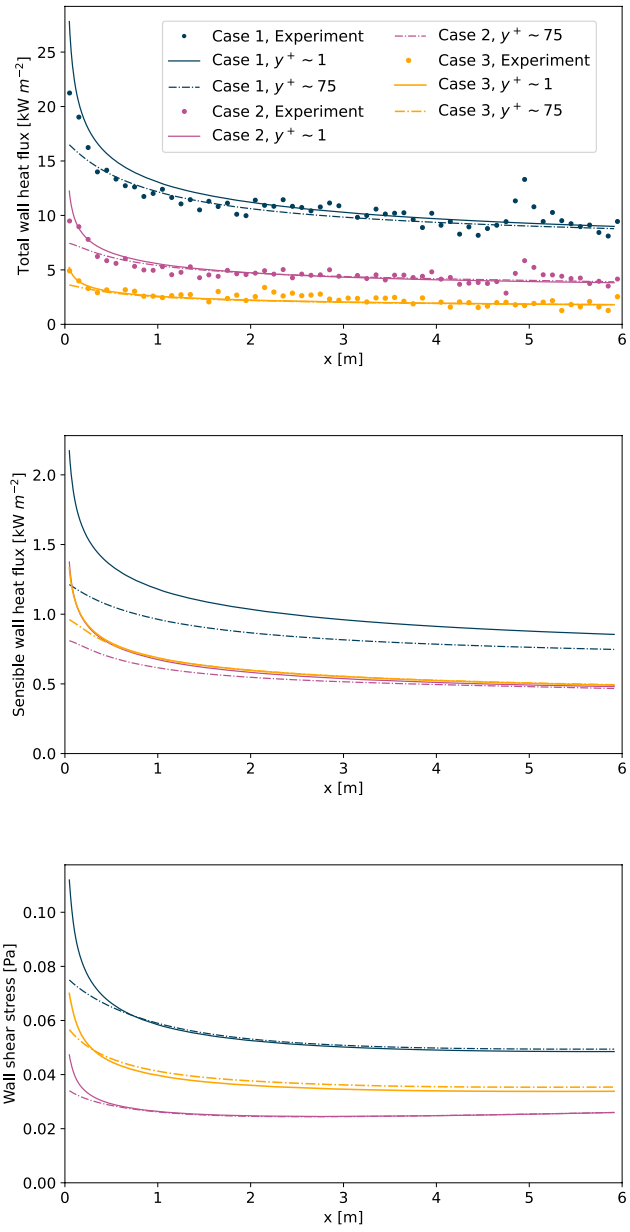

Figure 9: Local wall fluxes—total wall heat flux (top), convective wall heat flux (middle), wall shear stress (bottom)—along the condensing wall for three cases (differentiated by color) with the fine (solid line) and coarse (dotted-dashed line) meshes. Experimental data is available for the total wall heat flux only (dots).

5.4.2. Integral total wall heat flux

Figure 10 compares the experimental and simulated values of integral total wall heat flux, i.e., $\int_{x=0}^{6} \dot{q}''_{\text{total}}\, dx$, for all the experiments performed in the forced convection flow regime at the SETCOM facility. In total, 81 tests with a Reynolds number range of 70.000 - 100.000 and suction velocity v^{+}_{suc} of $-8.1 \cdot 10^{-3}$ to $-1.44 \cdot 10^{-2}$ is summarized. The fine mesh solutions are within an error band of $\pm 10\,\%$, with a few outliers in the $\pm 15\,\%$ range, which, however, is within the accuracy of the heat flux sensors itself. The coarse mesh results reveal a systematic under-prediction compared to the experimental data and the fine mesh solutions; this may again be attributed to the inefficacy of the wall functions for the developing part of the flow and the "suction effect."

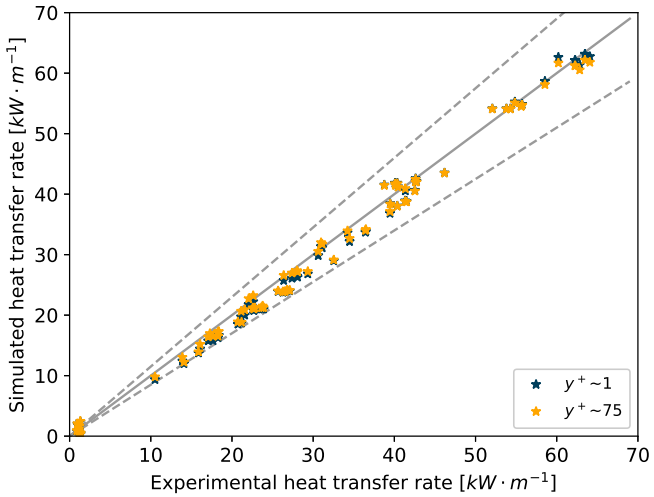

Figure 10: Comparison of the experimental integral heat flux with the fine mesh ($y^+ \sim 1$) and coarse mesh ($y^+ \sim 75$) solutions for 81 forced convection tests in the SETCOM facility. The dotted grey lines indicate a deviation of $\pm 15\,\%$ from the center line (solid grey line).

In conclusion, the model validity was proven for a broad range of flow parameters and condensation rates. The model presented exhibits mesh insensitive results for forced convection flows in the fully developed regions, confirming the validity of the chosen wall functions. During the validation studies, a sensi-

tivity to the inlet boundary conditions, especially the turbulence intensity and length scale at the inlet, was observed. A turbulent intensity value of $I = 10\,\%$, along with a length scale of 2.5 (channel width in the flow straightener), was found to provide the most consistent results when compared to the experimental database. Further experimental work will be carried out to characterize the inlet turbulence intensity accurately.

6. Summary and Conclusion

In the current work, a CFD model to predict the film condensation of vapor on walls in the presence of non-condensable gases is discussed in detail. The model was developed in the framework of *containmentFoam* solver based on open-source CFD code OpenFOAM with focus on application to nuclear reactor containment atmosphere mixing. The factors affecting wall condensation, i.e., condensate thermal resistance, the interfacial shear stress, thermal resistance at the interface, and the transport resistance in the diffusion boundary layer of the gas-phase due to the presence of non-condensable gases, are briefly presented. In the presence of non-condensable gases ($Y_{nc} > 10\,\%$), the dominant heat and mass transport resistance are in the diffusion boundary layer of the gas phase. Subsequently, the effects of the liquid film thermal resistance, shear stress at the liquid-vapor phase interface, and the interfacial thermal resistance were omitted; thus, the modeling of the two-phase condensation phenomenon simplifies into a single-phase (gas) problem.

Commonly, two approaches are used in the literature for modeling wall condensation in the presence of non-condensable gases model: In the first, *Volumetric source terms* model, the mass removed due to condensation and the corresponding transported quantities are specified with volumetric source (sink) terms in the control-volumes adjacent to the wall. Alternatively, the *Face-flux* method considers condensation by defining face fluxes, directed out of the domain, at the condensing interface. Wall condensation models available in the literature were primarily restricted to a binary mixture, e.g., steam-air. To

close the gap to a arbitrary multi-component non-condensable gas mixture, we extended the above two approaches ($\geq$ 2 species) and discussed the governing equations, boundary conditions and the numerical solution method in detail. The comparison of the performance of the two approaches, based on a two-dimensional channel flow test case, revealed for the first time that the *Face-flux* method proved to be superior on the counts of solution convergence rate, grid-independence and mass conservation.

Subsequently, a first validation the *Face-flux* model against the experimental data obtained at the SETCOM facility, for flows in the forced convection regime, was conducted. Overall, good agreement with experimental data was found for the total wall fluxes for three cases with paltry to severe condensation rates, on both the fine ($y^+ \sim 1$) and coarse ($y^+ \sim 75$) meshes. Since the wall functions used in the current work are derived for fully-developed forced convection flows, the coarse mesh solution compared reasonably with the fine mesh solution in the developed part of the flow but deviated in the developing flow. Also, for higher condensation rates, grid-dependency was observed because of the "suction effect," which tends to change the profile in the log part of the boundary layer. Finally, the model was compared against a complete forced convection SETCOM experimental database and yielded reasonable accuracy ($< \pm 10\,\%$ deviation in terms of the integral heat transfer rate).

Ongoing and future work aims at model application to flows in the mixed convection regime, which are expected inside the containment in the long term of the accident transient. This implies, in particular, an extension of the wall treatment for under-resolved boundary layers. In parallel, model validation against different separate effect tests and application-oriented large scale experiments is conducted to further substantiate the model and identify its limitations.

7. Acknowledgements

The authors gratefully acknowledge the German Federal Ministry for Economic Affairs and Energy for funding the development experimental and analyt-

ical work in the frame of the SETCOM project on "Experiments and CFD Model Development for Wall Condensation on Containment Structures" (Project No. 1501489, 1501591), which is conducted in close cooperation between Forschungszentrum Jülich GmbH and RWTH Aachen University. They also appreciate the DAAD-UGC for providing funding for the Joint Doctoral Program between IIT Madras and RWTH Aachen University.

References

Ambrosini W, Forgione N, Merli F, Oriolo F, Paci S, Kljenak I, Kostka P, Vyskocil L, Travis JR, Lehmkuhl J, Kelm S, Chin YS, Bucci M. Lesson learned from the SARNET wall condensation benchmarks. Annals of Nuclear Energy 2014;74(C):153–64. doi:10.1016/j.anucene.2014.07.014.

Antoine C. Tensions des vapeurs; nouvelle relation entre les tensions et les températures. Comptes Rendus des Séances de l'Académie des Sciences (in French) 1888;107:681–4.

Bucci M, Ambrosini W, Forgione N. Experimental and Computational Analysis of Steam Condensation in the Presence of Air and Helium. Nuclear Technology 2013;181(1):115–32. URL: https://www.tandfonline.com/doi/full/10.13182/NT13-A15761. doi:10.13182/NT13-A15761.

Cess RD. Laminar-film condensation on a flat plate in the absence of a body force. Zeitschrift für angewandte Mathematik und Physik ZAMP 1960;11(5):426–33. doi:10.1007/BF01604500.

Chilton TH, Colburn AP. Mass transfer (absorption) coefficients prediction from data on heat transfer and fluid friction. Industrial & engineering chemistry 1934;26(11):1183–7.

Corradini ML. Turbulent condensation on a cold wall in the presence of a noncondensable gas. Nuclear Technology 1984;64(2):186–95. doi:10.13182/NT84-A33341.

Dehbi A. A generalized correlation for steam condensation rates in the presence of air under turbulent free convection. International Journal of Heat and Mass Transfer 2015;86:1 – 15. doi:https://doi.org/10.1016/j.ijheatmasstransfer.2015.02.034.

Dehbi A, Janasz F, Bell B. Prediction of steam condensation in the presence of noncondensable gases using a CFD-based approach. Nuclear Engineering and Design 2013;258:199–210. URL: http://dx.doi.org/10.1016/j.nucengdes.2013.02.002. doi:10.1016/j.nucengdes.2013.02.002.

ERCOFTAC . European Research Community on Flow Turbulence and Combustion (ERCOFTAC) Best Practice Guidelines - Industrial Computational Fluid Dynamics of Single-Phase Flows, Version 1, 2001.

Favre A, Dumas R, Verollet E, Coantic M. Couche limite turbulente sur paroi poreuse avec aspiration. Journal de Mecanique 1966;5(1):3–28.

Fuller EN, Schettler PD, Giddings JC. New method for prediction of binary gas-phase diffusion coefficients. Industrial Engineering Chemistry 1966;58(5):18–27. doi:10.1021/ie50677a007.

Huang J, Zhang J, Wang L. Review of vapor condensation heat and mass transfer in the presence of non-condensable gas. Applied Thermal Engineering 2015;89:469–84. doi:10.1016/j.applthermaleng.2015.06.040.

Kader BA. Temperature and concentration profiles in fully turbulent boundary layers. International Journal of Heat and Mass Transfer 1981;24(9):1541–4. doi:10.1016/0017-9310(81)90220-9.

Kelm S, Kampili M, Gopala Krishna Moorthy VK, Sakamoto K, Liu X, Druska C, Kuhr A, Prakash K, Allelein HJ. Development and first validation of the tailored cfd solver 'containmentfoam' for analysis of containment atmosphere mixing. In: 18th International Topical Meeting on Nuclear Reactor Thermal Hydraulics (NURETH-18). Portland, Oregon, USA; 2019a. .

Kelm S, Müller H, Hundhausen A, Druska C, Kuhr A, Allelein HJ. Development of a multi-dimensional wall-function approach for wall condensation. Nuclear Engineering and Design 2019b;353:110239.

Koh J. Film condensation in a forced-convection boundary-layer flow. International Journal of Heat and Mass Transfer 1962;5(10):941–54. doi:10.1016/0017-9310(62)90074-1.

Koh JC, Sparrow EM, Hartnett JP. The two phase boundary layer in laminar film condensation. International Journal of Heat and Mass Transfer 1961;2(1-2):69–82. doi:10.1016/0017-9310(61)90015-1.

Kumar GV, Kampili M, Kelm S, Prakash KA, Allelein HJ. CFD modelling of buoyancy driven flows in enclosures with relevance to nuclear reactor safety. Nuclear Engineering and Design 2020;365:110682. doi:https://doi.org/10.1016/j.nucengdes.2020.110682.

Lehmkuhl J, Kelm S, Bucci M, Allelein HJ. Improvement of wall condensation modeling with suction wall functions for containment application. Nuclear Engineering and Design 2016;299:105–11. URL: http://dx.doi.org/10.1016/j.nucengdes.2015.08.002. doi:10.1016/j.nucengdes.2015.08.002.

Menter F, Esch T. Elements of industrial heat transfer prediction. In: Proceedings of the 16th Brazilian Congress of Mechanical Engineering (COBEM-2001). 2001. .

Minkowycz WJ, Sparrow EM. Condensation heat transfer in the presence of noncondensables, interfacial resistance, superheating, variable properties, and diffusion. International Journal of Heat and Mass Transfer 1966;9(10):1125–44. doi:10.1016/0017-9310(66)90035-4.

Nusselt W. Die oberflächenkondensation des wasserdampfes. Zeitschrift des Vereines Deutscher Ingenieure 1916;60(27):541–6.

Peterson PF, Schrock VE, Kageyama T. Diffusion layer theory for turbulent vapor condensation with noncondensable gases. Journal of Heat Transfer

1993;115(4):998–1003. URL: https://doi.org/10.1115/1.2911397. doi:10.1115/1.2911397.

de la Rosa JC, Escrivá A, Herranz LE, Cicero T, Muñoz-Cobo JL. Review on condensation on the containment structures. Progress in Nuclear Energy 2009;51(1):32–66. doi:10.1016/j.pnucene.2008.01.003.

Spalding DB. A Single Formula for the "Law of the Wall". Journal of Applied Mechanics 1961;28(3):455–8. URL: https://doi.org/10.1115/1.3641728. doi:10.1115/1.3641728.

Sparrow E, Minkowycz W, Saddy M. Forced convection condensation in the presence of noncondensables and interfacial resistance. International Journal of Heat and Mass Transfer 1967;10(12):1829–45. doi:10.1016/0017-9310(67)90053-1.

Sparrow EM, Gregg JL. A boundary-layer treatment of laminar-film condensation. Journal of Heat Transfer 1959;81(1):13–8. doi:10.1115/1.4008118.

Sucec J. Prediction of heat transfer in turbulent, transpired boundary layers. Journal of Heat Transfer 1999;121(1):186–90. URL: https://doi.org/10.1115/1.2825940. doi:10.1115/1.2825940.

Uchida H, Oyama A, Togo Y. Evaluation of post-incident cooling systems of light-water power reactors. In: Proceedings of the Third International Conference on the Peaceful Uses of Atomic Energy, Geneva, August 31–September 9, 1964. volume 13; 1965. p. 93 – 104.

Wilke CR. A Viscosity Equation for Gas Mixtures. The Journal of Chemical Physics 1950;18(4):517–9. URL: http://aip.scitation.org/doi/10.1063/1.1747673. doi:10.1063/1.1747673.

Zschaeck G, Frank T, Burns A. CFD modelling and validation of wall condensation in the presence of non-condensable gases. Nuclear Engineering and Design 2014;279:137–46. URL: https://linkinghub.elsevier.

com/retrieve/pii/S0029549314001393. doi:10.1016/j.nucengdes.2014.03.007.